Magnonic active ring co-processor

Special Collection: Recent Advances in Magnonics

Mykhaylo Balynsky ⁽¹⁾; Yuri Khivintsev ⁽¹⁾; Alexander Kozhevnikov ⁽¹⁾; Yuri Nikulin; Valentin Sakharov ⁽¹⁾; Yuri Filimonov ⁽¹⁾; Alexander Khitun ¹⁰ ⁽¹⁾ Check for updates

Journal of Applied Physics 133, 023904 (2023) https://doi.org/10.1063/5.0130423





CrossMark





Cite as: J. Appl. Phys. 133, 023904 (2023); doi: 10.1063/5.0130423 Submitted: 11 October 2022 · Accepted: 23 December 2022 ·

Published Online: 11 January 2023







Mykhaylo Balynsky, 1 📵 Yuri Khivintsev, 2 📵 Alexander Kozhevnikov, 2 📵 Yuri Nikulin, 2 Valentin Sakharov, 2 📵 Yuri Filimonov,^{2,3} 🕩 and Alexander Khitun^{1,a)} 🕩



AFFILIATIONS

Note: This paper is part of the Special Topic on Recent Advances in Magnonics.

ABSTRACT

In this work, we consider the possibility of building a magnonic co-processor for special task data processing. Its principle of operation is based on the natural property of an active ring circuit to self-adjust to the resonant frequency. The co-processor comprises a multi-path active ring circuit where the magnetic part is a mesh of magnonic waveguides. Each waveguide acts as a phase shifter and a frequency filter at the same time. Being connected to the external electric part, the system naturally searches for the path which matches the phase of the electric part. This property can be utilized for solving a variety of mathematical problems including prime factorization, bridges of the Konigsberg problem, traveling salesman, etc. We also present experimental data on the proof-of-the-concept experiment demonstrating the 🗧 spin wave signal re-routing inside a magnonic matrix depending on the position of the electric phase shifter. The magnetic part is a 3 × 3 8 matrix of waveguides made of single-crystal yttrium iron garnet $Y_3Fe_2(FeO_4)_3$ films. The results demonstrate a prominent change in the output power at different ports depending on the position of the electric phase shifter. The described magnonic co-processor is robust, & deterministic, and operates at room temperature. The ability to exploit the unique physical properties inherent in spin waves and classical wave superposition may be translated into a huge functional throughput that may exceed 1060 operations per meter squared per second for 50 50 magnetic mesh. Physical limits and constraints are also discussed.

Published under an exclusive license by AIP Publishing. https://doi.org/10.1063/5.0130423

I. INTRODUCTION

There is a permanent need in increasing the computational power of our computers. Nowadays, this need is associated mainly with the rapid development of the Internet of Things (IoT), bioinformatics,² as well as the growing size of datacenters (e.g., Google and Facebook). Modern computing devices consist of a large number of transistors assembled in Boolean logic gates.³ The structure of transistor-based Boolean logic gates remains mainly unchanged for the last 50 years. A major enhancement in the functional throughput is associated with scaling down the size of transistors and increasing their switching frequency.^{4,5} Complementary metal-oxide-semiconductor (CMOS) is currently the most elaborated transistor. However, a further scaling down of CMOS is associated with significant technological challenges.^{7,8} Power dissipation and chip overheating have appeared as grand problems. In turn, it stimulates a search for alternative solutions. The next generation of logic devices may be neither Boolean nor

transistor-based. There is a big room for the development of special task data processing devices that may complement CMOS.

Spintronic and multiferroic systems are among the promising candidates. 10 Magnonics is a budding research field in spintronics that addresses the use of spin waves (magnons) to transmit, store, and process information.¹¹ The first spin wave logic devices were proposed and demonstrated in 2005. 12,13 There has been significant progress since then in building different types of magnonic logic devices. 14-20 So far, most of the efforts have been focused on building transistor-like structures.²¹ It is unlikely that magnonic logic devices will compete with CMOS in speed and scalability. However, the unique combination of physical properties inherent in spin waves may be utilized for building memory and special task data processing devices. For example, spin wave based time-multiplexed Ising Machine has been recently demonstrated.²²

Here, we describe a Magnonic Active Ring co-Processor (MARcP), where an act of computation is associated with finding a

¹Department of Electrical and Computer Engineering, University of California—Riverside, Riverside 92521, California, USA

 $^{^2}$ Kotelnikov Institute of Radioengineering and Electronics of the Russian Academy of Sciences, Saratov 410019, Russia

³Physical and Mathematical Sciences, Saratov State University, Saratov 410019, Russia

^{a)}Author to whom correspondence should be addressed: akhitun@engr.ucr.edu

propagation path of a spin wave signal in a multi-path matrix. Active ring circuits with spin wave delay lines have been proposed for reservoir computing.²³ The principle of operation of the reservoir systems is based on strong nonlinearity and delayed response. Our approach is based on the superposition of states that is achieved in a multi-path active ring circuit. This approach is first described in Ref. 24. It is aimed to solve specific types of computational problems such as prime factorization, the bridges of Konigsberg, the traveling salesman problem, etc. The rest of the work is organized as follows. In Sec. II, we describe the material structure and the principle of operation of MARcP. The results of numerical modeling illustrating MARcP operation are presented in Sec. III. The experimental data obtained on the test six-port structure are presented in Sec. IV. The discussion and conclusions are given in Secs. V and VI, respectively.

II. MATERIAL STRUCTURE AND PRINCIPLE OF OPERATION

The schematics of MARcP are shown in Fig. 1(a). It is an active ring circuit comprising magnetic and electric parts. The magnetic part is a 2D mesh of magnetic waveguides made of materials with low spin wave damping [e.g., Y₃Fe₂(FeO₄)₃)]. These waveguides constitute a media for spin wave propagation. The electric part consists of a broadband amplifier G, a set of input and output switches to control the matrix connection with the electric part, and a set of voltage-controllable phase shifters Ψ_i and voltagecontrollable attenuators Ai, where the subscript i depicts the matrix row number. In Fig. 1(a), a 5 × 5 matrix with five input and five output switches is shown. The signal in the ring circuit circulates through the electric and magnetic parts exhibiting a transition from an electromagnetic wave (electric part) to a spin wave

(magnetic part) and vice versa. The conversion can be accomplished via micro antennas²⁵ or multiferroic elements.²⁶ These elements are placed at each input and output port of the matrix.

In Fig. 1(b), it is schematically shown, the structure of the magnonic matrix. The core of the structure is a 2D mesh of magnonic waveguides where spin waves propagate. There are multiferroic elements (e.g., synthetic multifferoics²⁷) placed on top of the waveguide junctions. These elements are aimed to provide a voltage-controllable local magnetic field. As the spin wave dispersion depends strongly on the bias magnetic field, 28 the combination of synthetic multiferroic and waveguide acts as a delay line and a tunable frequency filter for spin waves. The phase change accumulated by the spin wave propagating under the multiferroic element depends on the strength and the direction of the magnetic field (i.e., the applied voltage). Overall, the magnetic part can be considered as a mesh of delay lines and frequency filters, where different propagation paths may differ in the phase shift and attenuation for a given frequency. There are also power detectors placed on top of the waveguides between the junctions. For example, it may be Inverse Spin Hall Effect (ISHE) detectors. These detectors are aimed to provide the output: the signal propagation route.

The principle of operation is based on the appealing property of an active ring circuit to self-adjust to the resonant frequency enabling auto-oscillations. There are two conditions for auto-oscillations to occur in an active ring circuit,29

$$G A L(f) 1,$$
 (1:1)

Ψ b
$$\Delta(f)$$
 ¼ $2\pi k$, where k ¼ 1, 2, 3, ..., (1:2) $\vec{\Rightarrow}$

where G is the gain provided by the amplifier, L(f) is the signal attenuation in the matrix, A is the signal attenuation in the electric $\frac{800}{100}$

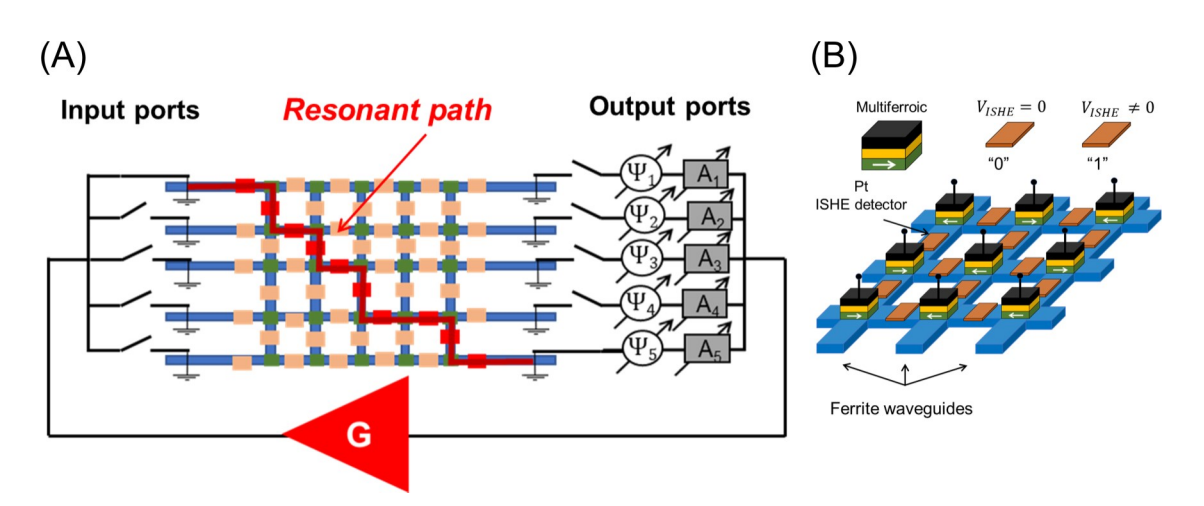


FIG. 1. (a) Schematics of MARcP. It is an active ring circuit comprising electric and magnetic parts. The electric part consists of a broadband amplifier G, a set of input and output switches to control the matrix connection with the electric part, and a set of voltage-controllable phase shifters Ψ and voltage-controllable attenuators A. The magnetic part is a 2D mesh of magnetic waveguides. An act of computation is associated with finding a path(s) through the matrix depending on the set of external phase shifters and attenuators. (b) Schematic view of the magnonic matrix. It is a 2D mesh of magnonic waveguides. There are multiferroic elements placed on top of the wave-guide junctions. There are also power detectors (e.g., ISHE) placed on top of the waveguides between the junctions. These detectors are to detect the spin wave propaga-tion path(s).

part, $\Delta(f)$ is the phase shift of the matrix, and Ψ is the phase shift of the electric part. Both the attenuation and the phase shift depend on the signal frequency f. The first equation (1.1) states the amplitude condition for auto-oscillations: the gain provided by the broadband amplifier should be sufficient to compensate for losses in the passive magnetic matrix and losses introduced by the attenuator(s). The second equation states the phase condition for auto-oscillations: the total phase shift for a signal circulating through the ring should be a multiple of 2π : In this case, signals come in phase every propagation round. A more rigorous description of signal propagation in magnonic active ring circuits can be found in Ref. 29. Different paths in the magnonic matrix may provide different phase shifts, attenuation, and, most importantly, support different signal frequencies. Thus, only signals propagating in the resonant path(s) in the matrix will be amplified in the active ring circuit. A more detailed explanation of the selective signal amplification in a multi-path active ring circuit can be found in Ref. 24.

The computational procedure is the following. The set of multiferroic elements is initialized (i.e., biased) prior to computation. It is assumed that each of the elements has an individual contact which allows us to control the applied voltage at each junction. The bias voltage is fixed during the computation. The mutual arrangement of the multiferroic elements defines the phase shift/attenuation/frequency for the different paths in the matrix. Overall, the matrix can be considered as a database where information is encoded in the signal propagation route. The instructions are encoded in the position of the switches connecting the electric and magnetic parts, and the set of phase shifters Ψ_i and voltagecontrollable attenuators Ai. For example, one can instruct the system to find the path(s) connected to input port #1 and output port #5 that provides a phase shift of 0:25π. The phase shifter at output #5 should be set to $\Psi_5 \frac{1}{4} 2\pi 0:25\pi \frac{1}{4} 1:75\pi$. Then, it may be possible to find the path with minimum losses out of all possible using the attenuator A₅.

As soon as the magnonic matrix is connected to the electric part, the system starts to adjust to the resonant frequency(s) at which conditions (1.1) and (1.2) are met. The system starts with a superposition of all possible frequencies circulating in the ring through all possible paths. However, only signals propagating through the resonant path(s) will be amplified. A more detailed description of the amplification process can be found in Ref. 24. This process of self-adjustment manifests itself in spin wave propagation route change depending on the external phase shifter. That is the key property of the multi-path active circuit to be exploited for logic functionality. In the next section, we present the results of numerical modeling illustrating the signal re-routing through the matrix depending on the external phase shifter.

III. NUMERICAL MODELING

In order to illustrate the principle of operation of MARcP, we present the results of numerical modeling for an active ring circuit with a 3×3 magnetic matrix as shown in Fig. 2. To simplify our consideration, we consider only one phase shifter and one attenuator in the electric part. Also, we consider all three side switches to be in the "On" position. The green boxes in Fig. 2

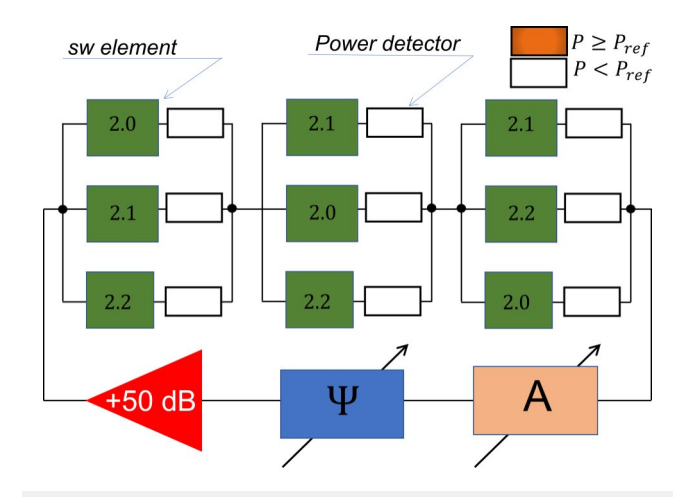


FIG. 2. Schematics of the active ring circuit with 3×3 magnetic matrix. The matrix consists of nine elements arranged in three columns with three elements per column. The elements are shown as green boxes. The number in each box corresponds to the central frequency f_0 . Each of the elements is accompanied with a power detector. The color of the detector is brown if the transmitted power exceeds some reference value P_{ref} . The color of the detector is white otherwise.

depict spin wave elements that provide frequency-dependent phase shift and frequency-dependent attenuation to the propagating spin waves. There are nine elements assembled in three columns with three elements per column. Each of the spin wave elements is accompanied by a power detector. The color of the detector is brown if the transmitted power exceeds some reference value P_{ref} . The color of the detector is white otherwise. Our objective is to show the change in signal propagation through the amatrix depending on the position of the external phase shifter (hereafter, the external phase).

To model the phase delay and the frequency-dependent attenuation, we use the characteristics of commercially available voltage-controllable filters based on the YIG delay line produced by Micro Lambda Wireless, Inc, model MLFD-40540. The experimental data are shown in Fig. 3. The transmission [Fig. 3(a)] and the phase delay [Fig. 3(b)] in the frequency range from 2.2 to 3.8 GHz with a central frequency of 3.0 GHz are shown. The central frequency is controlled by the applied voltage in the range from 0.5 to 4.0 GHz. The transmission is well-fitted by the Lorentzian function as follows:

$$L(f) \frac{1}{\pi} = \frac{\frac{1}{2}\Gamma}{\tilde{\sigma}_f f_0 p^2 p} \frac{1}{2^{\frac{1}{L}}}$$
 (2)

where f_0 is the center frequency and Γ is a parameter specifying the width at the half height. It was taken Γ ½ 0:2 GHz in numerical modeling. The phase shift was approximated by the peace-wise characteristic. The fitted transmission and phase are shown in Figs. 3(c) and 3(d), respectively. The central frequency for each

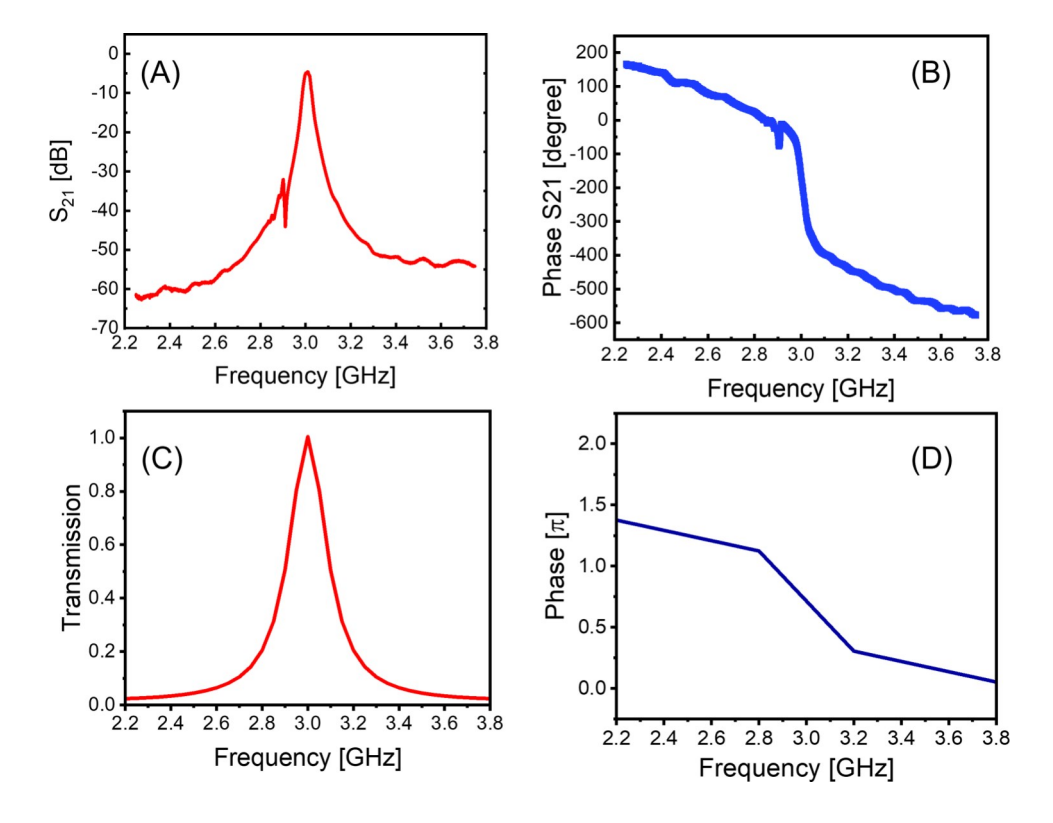


FIG. 3. (a) Experimental data: S21 parameter (amplitude) of the commercial filter. (b) Experimental data: S21 parameter (phase shift) of the commercial filter. (c) Results of numerical fitting: transmission of the spin wave element. (d) Results of numerical fitting: phase shift produced by the spin wave element. The data are shown in the frequency range from 2.2 to 3.8 GHz.

element can be individually adjusted. The numbers in the green boxes in Fig. 2. show the central frequency for each element.

In order to find the paths satisfying the self-oscillation conditions, we calculate matrix response for a given frequency in the frequency range from 1 to 3 GHz. There are three steps for each given frequency. (i) The signal attenuation L(f) and the phase delay $\Delta(f)$ are calculated for the complete matrix. (ii) The calculated L(f) and $\Delta(f)$ are checked to satisfy the auto-oscillation conditions (1.1) and (1.2). (iii) If the auto-oscillation conditions are met, one finds the signal propagation path (the distribution of the signal power within the matrix).

Step (i) starts with the calculation of attenuation L_{i,i}(f) and phase shift $\Delta_{i,i}(f)$ for all nine elements in the matrix, where subscripts i and j denote the column and the row numbers, respectively. Next, we calculate the attenuation and the phase shift for each column in the matrix. The calculation procedure is the following. First, we calculate the real and imaginary components of the spin wave signal passing through all elements in the first column,

$$\begin{split} &\text{Re}[L_1(f)] \; \% \quad \stackrel{P}{\underset{j \not \bowtie 1, n}{\text{pr}}} L_{i,j}(f) \; \cos[\Delta_{i,j}], \\ &\text{Im}[L_1(f)] \; \% \quad \stackrel{j \not \bowtie 1, n}{\underset{j \not \bowtie 1, n}{\text{pr}}} L_{i,j}(f) \; \sin[\Delta_{i,j}], \end{split} \tag{3} \end{split}$$

where M_{1x} and M_{1y} are the components after the first column, the summation is over all elements in the column. Second, we calculate the transmission and the phase shift introduced by the first

column,

Third, the attenuation and the phase shift produced by the whole matrix are calculated as follows:

where the subscripts denote the column number. In step (ii), conditions (1.1) and (1.2) are checked for the calculated L(f) and $\Delta(f)$. Step (iii) is accomplished if the self-oscillation conditions are met. The distribution of signal power is calculated based on the known L_{i,j}(f). The power splits between the elements in each column are proportional to the element transmission. This calculation procedure can be extended to any size of the matrix.

In Fig. 4, the results of numerical modeling showing the phase shift $\Delta(f)$ are shown and the attenuation L(f) of the matrix in the frequency range from 1.0 to 5.0 GHz is shown in Fig. 2. These data shown in a 3D plot show the relationship between the frequencyphase-attenuation for the whole matrix. It is important to note that each point in the 3D plot is associated with some propagation path (s). The frequency of auto-oscillations depends on the electric part phase and attenuation.

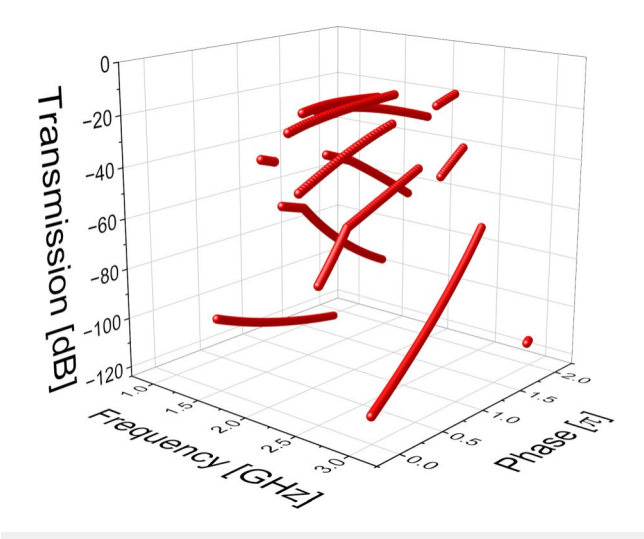


FIG. 4. Results of numerical modeling showing the phase delay and the attenuation of the matrix shown in Fig. 2. The parameters are calculated in the frequency range from 1.0 to 3.0 GHz.

To illustrate the change in the signal propagation route, we show several schematics of the circuit with power detectors for different positions of the external phase shifter Ψ . The amplifier is taken to provide +50 dB frequency-independent amplification in the whole frequency range. The attenuator is set to -35 dB. The

reference power for the power detectors is set to P_{ref} ¼ 5 dBm. In Fig. 5, the sequence of circuit schematics illustrating the change in the propagation path depending on the phase shifter Ψ is shown. In Fig. 5(a), the case for $\Psi \% 0:0\pi$ is shown. There are no auto-oscillations, as there are no paths in the matrix to satisfy conditions (1.1) and (1.2). All power detectors are shown in white color. There are no auto-oscillations for $\Psi \%$ 0:4 π as illustrated in Fig. 5(b). This regime without auto-oscillation remains till the external phase exceeds 0.75π . In Fig. 5(c), the case for $\Psi \% 0.8\pi$ is shown. There are five power detectors revealing power flow in which magnitude exceeds the reference one. It indicates auto-oscillations in the circuit which may occur on one or several resonant frequencies. These frequency(s) are of no interest but only the propagation path is the result of the computation. There are 29 possible combinations (e.g., On/Off) for the nine power detectors. The circuit self-adjusts to the resonant path taking one path out of all possible. The signal path changes when the external phase is further increased. In Fig. 5(d), the case for $\Psi \%$ 1:1 π is shown. Almost all power detectors show power flow. In Fig. 5(e), the case for $\Psi \%$ 1:2 π is shown. Three of the power detectors become inactive compared to the case $\Psi \%$ 1:1 π : The auto-oscillations disappear as the phase exceeds Ψ ¼ 1:8π: All power detectors are shown in white color for the case $\Psi \% 2:0\pi$ as shown in Fig. 5(f). The system has returned to the initial state as in Fig. 5(a).

These results are aimed to illustrate the signal re-direction within the magnonic matrix depending on the external phase shifter. The results are shown for just one-input and one-output port. The central frequencies for the spin wave elements are arbitrarily chosen. In general, there is a plethora of possible

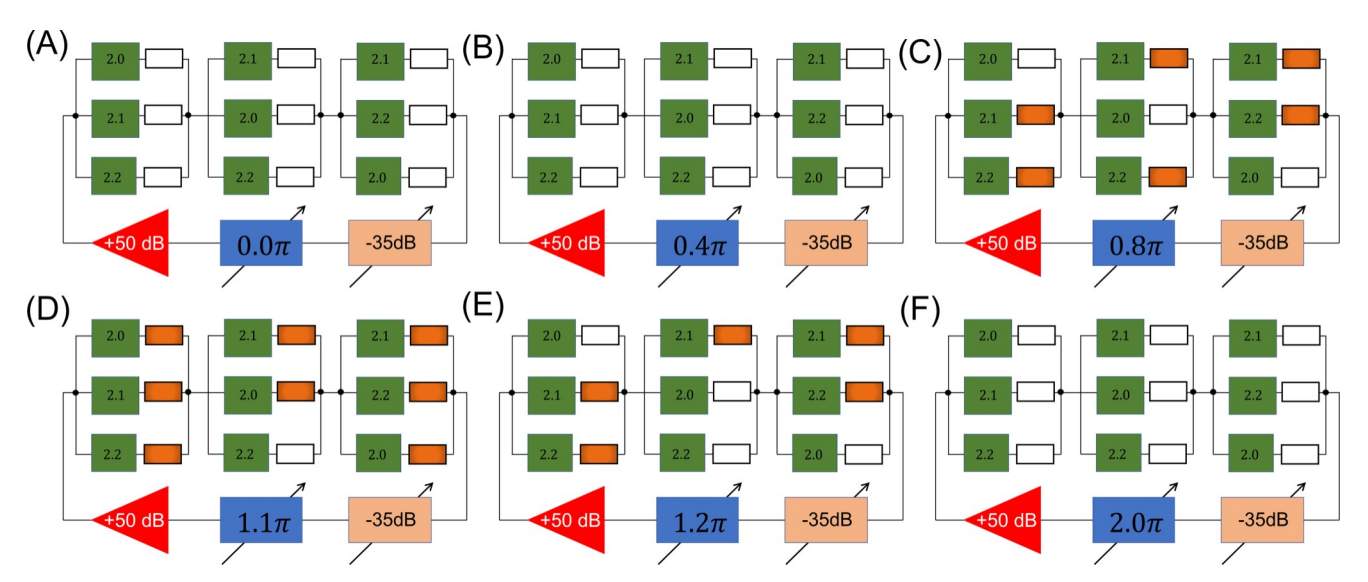


FIG. 5. Results of numerical modeling illustrating the change in the signal propagation path depending on the phase shifter Ψ . The amplifier is set to +50 dB while the attenuator is set to -35 dB. (a) The external phase is set to Ψ % 0:0 π . There are no auto-oscillations. None of the power detectors detects a power flow. (b) The external phase is set to Ψ % 0:0 π . There are no auto-oscillations for Ψ % 0:8 π . The set of color power detectors depicts the signal propagation path. (d) Propagation path for Ψ % 1:1 π . There are auto-oscillations but the propagation path is different compared to the previous case. (e) Propagation path for Ψ % 1:2 π . The set of power detectors shows the change in the signal propagation route. (f) The external phase is set to Ψ % 2:0 π . There are no auto-oscillations. None of the power detectors detects a power flow.

combinations to arrange spin wave elements in the matrix and to set up their phase shifts and frequency-dependent attenuation. There is also a large number of possible instructions to apply. In all cases, the active ring circuit will search for the resonant paths that will be amplified.

IV. EXPERIMENTAL DATA

In this part, we present experimental data showing spin wave signal re-routing in the multi-terminal active ring circuit. In Fig. 6, the top view of the test six-port structure is schematically shown. The core of the structure is a single-crystal yttrium iron garnet Y₃Fe₂(FeO₄)₃ (YIG) film of thickness 7 μm grown on a gallium gadolinium garnet (GGG) substrate by liquid phase epitaxy. The saturation magnetization of the film is $4\pi M_0 = 1750$ G. The YIG film was patterned using laser ablation to have a 2D mesh of the 3 × 3 orthogonal YIG waveguides 0.3 mm in width and 2.9 mm in length each. Then, the contact pads between the YIG waveguides as well as the wires over the YIG waveguides connecting these contact pads were fabricated out of copper on the sides of the structure using magnetron sputtering, photolithography, and ion etching. The blue color depicts the YIG material while the white color depicts the patterned area (i.e., the GGG substrate). The gold and black squares at the edges of the structure depict the contact pads. The size of each pad is about $0.5 \times 0.5 \text{ mm}^2$. The distance between the nearest pads is 0.3 mm. The pads are connected via conducting microstrips as depicted by the green color. The width of the microstrips is 0.045 mm. The black squares correspond to the ground

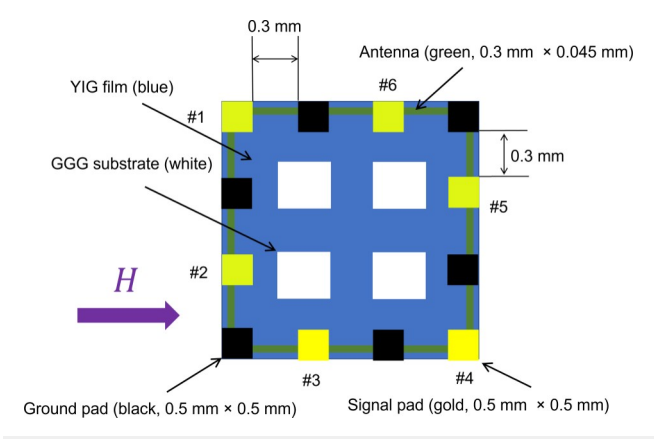


FIG. 6. Schematics of the test six-port structure. It has a square shape with the length of the side about 2.9 mm. The core of the structure is a single-crystal yttrium iron garnet Y₃Fe₂(FeO₄)₃ (YIG) film of thickness 7 μm. The saturation magnetization of the film is $4\pi M_0$ = 1750 G. The film is fabricated on top of the GGG substrate and patterned to have a 2D mesh of waveguides. The blue color depicts the YIG material while the white color depicts the patterned area (i.e., the GGG substrate). The gold and black squares at the edges of the structure depict the contact pads. The size of each pad is about $0.5 \times 0.5 \text{ mm}^2$. The distance between the nearest pads is 0.3 mm. The pads are connected via a conducting wire as depicted by the green color. The diameter of the wire is 0.045 mm. The black squares correspond to the ground pads while the gold contacts correspond to the signal pads. The green wires connecting the gold and the nearest black pads work as an antenna.

pads while the gold contacts correspond to the signal pads. The green microstrips connecting the gold and the nearest black pads work as an antenna. AC in the microstrip generates a time-varying magnetic field around the wires. Spin waves are excited when in resonance with the oscillating magnetic field. The same antennas can be utilized to convert the time-varying magnetic field produced by spin waves into AC voltage. The details on spin wave excitation and detection by micro antennas can be found elsewhere. 25,30 The structure is placed on top of a permanent magnet K&J Magnet, model BX8X84 which provides a constant bias in-plane magnetic field as shown in Fig. 6. The strength of the bias field is controlled by the space gap between the magnet and the test structure.

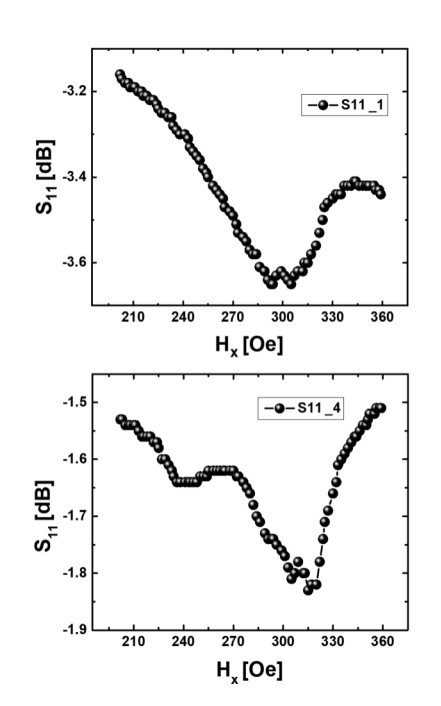
To find the optimum bias magnetic field, the structure was first tested using a programmable network analyzer (PNA Keysight N5241A). In Fig. 7, experimental data are shown: the S11 parameter measured at six input ports depending on the bias magnetic field H. The frequency is fixed to f 1/4 2:1 GHz. Spin wave excitation is accompanied by a decrease in the RF signal reflection, where a portion of the input power is transferred into a spin wave. There is a dip in the reflection power around H 1/4 300 Oe observed for all six ports. This bias magnetic field was fixed for the rest of the experiments.

We accomplished three experiments with different combinations of input/output ports with and without additional frequency filters. The schematics of experiment 1 are shown in Fig. 8. The sixterminal device is integrated within an active ring circuit via ports #1 and #4. The signal circulates clockwise through the circuit. The input port is #1 while the output port is #4. The micro antenna at port #1 converts the incoming electromagnetic wave of frequency f into a spin wave of the same frequency. The speed of spin wave \(\xi \) propagation is much slower compared to an electromagnetic wave 8 (e.g., about 10⁴ m/s for the given structure) which results in a significant phase shift for the propagating spin wave. Spin wave(s) reaching port #4 are converted into an electromagnetic wave using the same type of micro antenna. The electric part consists of a broadband amplifier and a phase shifter. The amplifier actually consists of three amplifiers connected in series, where each of the amplifiers can provide amplification of about 21 dB and output power of up to 20 dBm in the frequency range of 0.5-8.0 GHz. It should be noted that special measures were taken to limit the power in the circuit. The power limit is not due to the nonlinear processes in the YIG film but due to the saturation of the last amplifier in the chain of three. There are also three phase shifters connected in series where each of the shifters can provide a phase shift from 0π to $2:0 \pi$ at frequency 3.0 GHz. For simplicity, both the composite amplifier and the composite phase shifter are depicted as a single device. The circulating power can be measured in the entire circuit (i.e., P₀) and separately at each of the five outputs (i.e., P2, P3, P4, P5, and P6) as shown in Fig. 8. The external phase Ψ is gradually changed during the experiment. The change in the spin wave propagation path through the structure is detected by measuring the electric power at the output ports.

In Fig. 9(a), there are experimental data showing the frequency of the auto-oscillations in the ring circuit depending on the external phase Ψ . It is observed just one frequency branch that decreases from 2.595 to 2.565 GHz in the phase range from zero to 2:0 π. There is a jump to approximately the same starting value

S₁₁[dB]

S₁₁[dB]



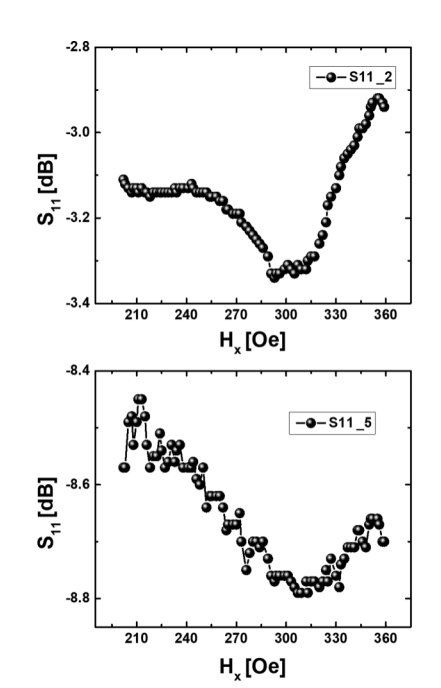


FIG. 7. Experimental data: a collection of six plots showing the S11 parameter measured at six input ports depending on the bias magnetic field H. The magnetic field is applied in-plane as shown in Fig. 6. The frequency is fixed to f ½ 2:1 GHz. The dip in the reflection spectra reflects spin wave excitation in the structure.

after $\Psi \% 2:0 \pi$. The frequency starts to decrease at the same rate as at the beginning of the measurements. However, the coming back phase is not exactly 2:0 π as one would expect. There is an additional phase shift (e.g., positive or negative) that is introduced

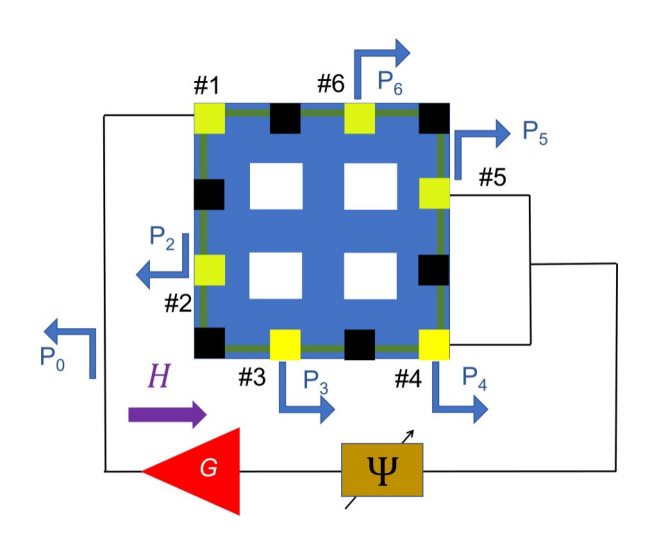
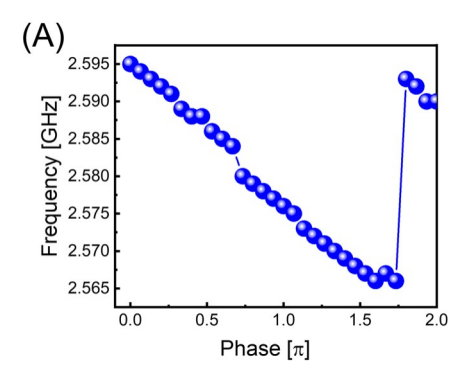
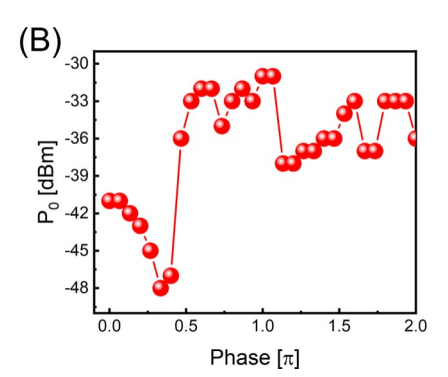


FIG. 8. Schematics of experiment 1. The six-terminal device is integrated into an active ring circuit via ports #1 and #4. The input port is #1 while the output port is #4. The external phase shifter Ψ can be changed from 0 to 2π . The cir-culating power can be measured in the entire circuit (i.e., P_0) or/and separately (P_i , i ½ 2, ::, 6) at each of the five outputs (i.e., P_2 , P_3 , P_4 , P_5 , and P_6).

by the other parts in the circuit. It should be also noted that the $\stackrel{\rightarrow}{=}$ phase shift produced by the phase shifter differs for different frequencies. So, the same divisions (i.e., rotation of the phase shifter) produce slightly different phase shifts on different frequencies. It $\frac{\omega}{\varpi}$ explains the slight deviation from 2:0 π periodicity for the measurement cycle. In Fig. 9(b), there are experimental data showing the $\stackrel{\omega}{=}$ power of auto-oscillations P_0 depending on the external phase Ψ . The power changes significantly from -30 dBm at the maximum to -48 dBm at the minimum. It reflects the change in the matrix attenuation for the different propagation paths. In Fig. 10(a), raw data on the output power measured at five output antennas #2-#6 depending on the external phase Ψ are shown. There are five curves of different colors where the color depicts the output power at different ports. The black, red, blue, pink, and green curves depict P₂, P₃, P₄, P₅, and P₆, respectively. On a first look, the output power measured at different output ports is almost the same and repeats the total power as shown in Fig. 9. However, a more detailed analysis reveals the difference for different antennas. In Fig. 10(b), the normalized data are shown. The normalization was accomplished for each output using the following formula: $P_i(\Psi) \ ^{\prime} P^r(\Psi) \ P^r(0) \ [P_0(0) \ P_0(\Psi)]$, where $P^r(\Psi)$ is the raw data of power at the ith output at phase Ψ , $P^{r}(0)$ $P_{0}(0)$ is the raw data of power at the ith output at phase 0π , $P_0(\Psi)^1$ and $P_0(0)$ are total power in the ring circuit at phase Ψ and phase 0π , respec-tively. There are several dBm differences between the output ports depending on the external phase Ψ . The maximum power comes through different output ports for different phases. For instance, most of the output power comes to port #2 at Ψ less than 0:45 π . The maximum of the output power shifts to output port #3 as the



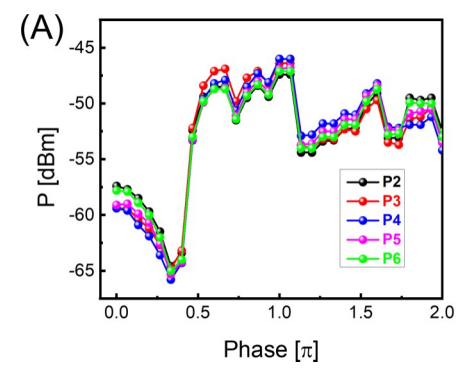


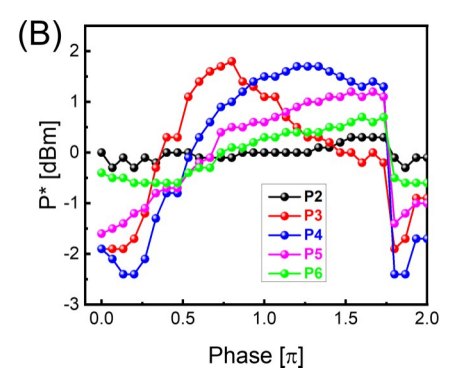
9. Experiment (a) Experimental data: the frequency of auto-oscillations as a function of the external phase Ψ . (b) Experimental data: the power of auto-oscillations Po as a function of the external phase Ψ .

phase exceeds 0:45 π . Port #4 receives most of the power for Ψ in the range from 0:5 π to 1:75 π . These changes in the output power indirectly reflect the signal re-direction within the matrix.

The schematics of experiment 2 are shown in Fig. 11. There are two input ports (i.e., port #1 and port #2) and two output ports (i.e., port #4 and port #5). There is an additional element—a commercial frequency filter produced by Micro Lambda Wireless, Inc. model MLFD-40540 that is incorporated in the circuit. The central frequency of the filter is 2.504 GHz. The signal circulates clockwise through the circuit. The circulating power can be measured in the entire circuit (i.e., P₀) and separately at each of the four outputs (i.e., P₃, P₄, P₅, and P₆). As in previous example 1, the external phase Ψ is gradually changed and output power is measured for different phases. In Fig. 12(a), there are experimental data showing the frequency of auto-oscillations in the ring circuit depending on the external phase Ψ . It is observed in just one frequency branch that decreases from 2.511 to 2.501 GHz in the phase range from zero to Ψ ¼ 1:70π. There is a gap in auto-oscillations for the external phase from 1.70π to 1.80π . There are no auto-oscillations for these external phases as none of the paths in the matrix satisfy conditions (1.1) and (1.2). The auto-oscillations appear again as the external phase exceeds 1:80π. The frequency of the auto-oscillation returns to the starting value for $\Psi \% 2:0\pi$. In Fig. 12(b), experimental data on the power of auto-oscillations P₀ depending on the position of the external phase shifter Ψ are shown. The power changes significantly from -6 dBm at the maximum to -18 dBm at the minimum. There is a gap in the power graph for the external phase from 1.70π to 1.80π , which confirms the absence of

auto-oscillations. The auto-oscillations appear again as the external phase exceeds 1:80π: In Fig. 13, raw data for the output power measured at the ports P3, P4, P5, and P6 are shown. It mainly repeats the data in Fig. 12(b). However, the power flow exhibits a prominent redistribution among the output ports depending on the external phase. Most of the power flow changes from port #5 to port #3 to port #4 as the external phase changes from zero to $0.5\pi^{\circ}$. There is no output power coming from any port for the external phase from $1:70\pi$ to $1:80\pi$. There is a redistribution of the output power as the auto-oscillations appear after 1:80π. In Fig. 14, raw data for the output power measured at the ports when only one-input port (i.e., either port #1 or port #2 in Fig. 11) is connected to the electric part are shown. In Fig. 14(a), data for input port #1 are shown. The output power is measured at ports -P₂, P₃, P₄, P₅, and P₆: The data in Fig. 14(a) match well with the ones in Fig. 13. However, the power distribution between the soutput ports is different. There is a prominent signal re-direction between ports #2, #4, and port #6. In Fig. 14(b), data for the case $\frac{\overline{\omega}}{N}$ when only input port #2 is connected to the electric part are & shown. The output power is measured at ports P1, P3, P4, P5, and P₆. The data differ drastically from the ones shown in Figs. 13 and 14(a). There is a completely different trend in the power distribution between the ports. There is no gap in the output power for the external phase from 1.70π to 1.80π ! On the one hand, it looks counter-intuitive - the more input ports are connected, the more possible paths are available for the spin wave signal. On the other hand, attenuation of the matrix depends on the phase difference between the spin waves coming to the outputs. It may happen that





10. Experiment (a) Experimental data (raw data) on the output power measured at five output antennas #2-#6 as a function of the external phase Ψ . The five curves of different colors depict the output power at different ports. The black, red, blue, pink, and green curves depict P₂, P₃, P₄, P₅, and P₆, respectively. (b) Data normalized assuming constant power in the ring.

FIG. 11. Schematics of experiment 2. The six-port device is integrated into an active ring circuit via two input ports #1 and #2 and two output ports #4 and #5. There is an additional frequency filter incorporated in the circuit. The power is measured in the entire circuit (i.e., P₀) and separately at each of the four outputs (i.e., P₃, P₄, P₅, and P₆).

the signals coming from port #1 and port #2 cancel each other (i.e., the destructive interference) when both input ports are connected. There is no destructive interference in the case of just one-input port #2. Thus, the output power in the case of two inputs connected in parallel cannot be considered as a simple sum of two inputs working separately (i.e., one at a time). It is important for estimating the number of possible instructions for MARcP.

The schematics of experiment 3 are shown in Fig. 15. There are three input ports (i.e., port #1, port #2, and port #3) and three output ports (i.e., port #4, port #5, and port #6). There are three frequency filters Micro Lambda Wireless, Inc, model MLFD-40540 incorporated for each of the output ports. The central frequency for the filter at port #4 is 2.467 GHz. The central frequency for the filter at port #5 is 2.484 GHz. The central frequency for the filter at port #6 is 2.592 GHz. The circulating power can be measured in the entire circuit (i.e., P₀) and separately at each of the four outputs (i.e., P₄, P₅, and P₆). In Fig. 16(a), there are experimental data

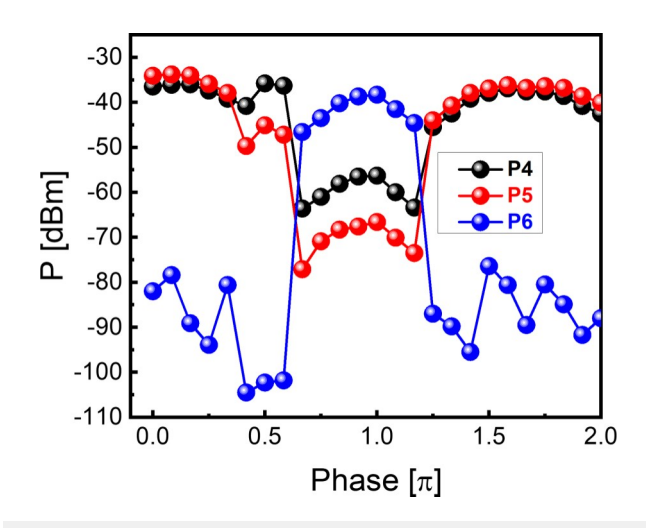
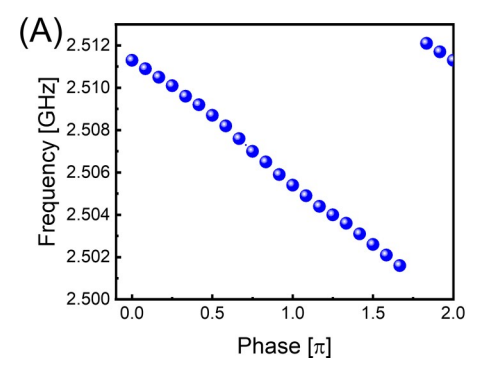
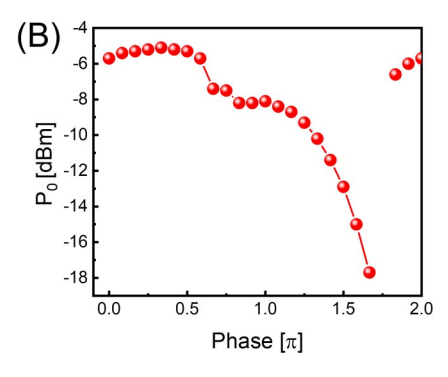


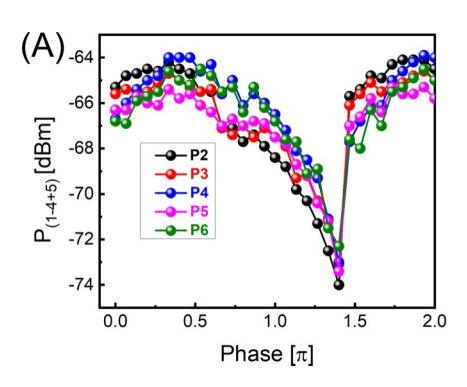
FIG. 13. Experiment 2. Experimental data: the output power measured at the ports as a function of the external phase shifter Ψ . The black, red, blue, and pink curves depict P₃, P₄, P₅, and P₆, respectively.

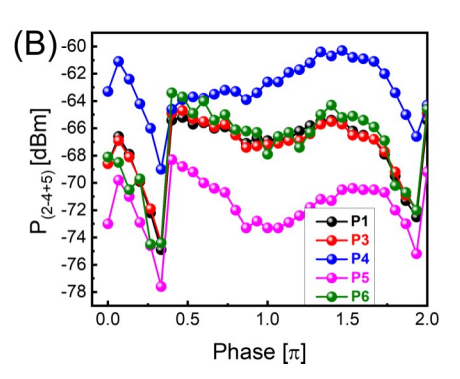
showing the frequency of auto-oscillations in the ring circuit depending on the position of the external phase Ψ . It clearly shows three frequency branches each around the central frequency of the filter. The jumps from one branch to another are quite stip. There is no phase region where two or three frequency branches coexist = at the same time. In Fig. 16(b), there are experimental data showing the power of auto-oscillation P_0 depending on the external phase Ψ . The power changes significantly from +0.5 dBm at the $\frac{3}{2}$ maximum to -19 dBm at the minimum. The evolution of the $\frac{30}{80}$ output power correlates with the change in the frequency of $\frac{30}{40}$ auto-oscillations. In Fig. 17, there are experimental data showing the output power measured at ports #4, #5, and #6 as a function of the external phase shift. The measurements are accomplished after the filters. There are three curves of different colors depicting the power at each of the outputs. The magnitude of the power changes in the range from -35 to -105 dBm. The switching between the outputs is clearly observed. For instance, the difference between ports #4 and #6 may exceed 40 dBm. The difference between ports #4 and #5 is much smaller. It can be well explained by the





12. Experiment Experimental data: the frequency of auto-oscillations in the ring circuit as a function of the external phase shifter Ψ. (b)Experimental data: the power of auto-oscillations P₀ as a function of the external phase shifter Ψ.





14. Experiment Experimental data for input port #1: the output power measured at the ports as a function of the external phase shifter Ψ. The black, red, blue, pink, and green curves depict P2, P3, P4, P5, and P_6 , respectively. (b) Experimental data for input port #2: the output power measured at the ports as a function of the external phase shifter Ψ . The black, red, blue, pink, and green curves depict P_1 , P_3 , P_4 , P_5 , and P_6 , respectively.

difference in the output filters. The central frequencies of the filters at ports #4 and #5 are close to each other. The output port #6 has the most difference in the transmission compared to ports #4 and #5. We want to emphasize the huge difference in the signal propagation path depending on the external phase. It is more than sufficient for a reliable path recognition. All measurements in this work are accomplished at room temperature.

V. DISCUSSION

There are several observations we would like to make based on the presented data. First of all, both the experimental data and the results of numerical modeling confirm the spin wave re-routing within the matrix governed by the external phase shifter. This is the keystone for the proposed MARcP operation. Though active ring circuits with spin wave delay lines have been on the stage for decades,³¹ signal re-direction in a multi-path configuration is mainly unexplored. The system naturally searches for the resonant

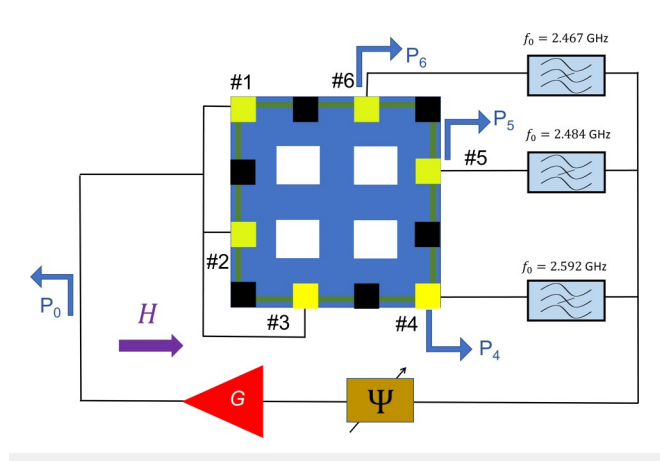


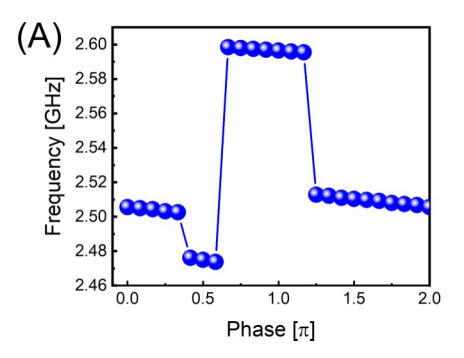
FIG. 15. Schematics of experiment 3. There are three input ports (#1, #2, and #3) and three output ports (#4, #5, and #6). There are three frequency filters incorporated into each of the output ports. The central frequency for the filter in port #4 is 2.467 GHz. The central frequency for the filter in port #5 is 2.484 GHz. The central frequency for the filter in port #6 is 2.592 GHz. The circulating power can be measured in the entire circuit (i.e., P₀) and separately at each of the four outputs (i.e., P4, P5, and P6).

path(s) inside the magnonic matrix depending on the external phase shifter. This phenomenon is very promising for logic and memory applications. It may be also utilized for addressing nanomagnets without the use of switches. Second, there is plenty of signal paths even in a small matrix. There are multiple paths connecting the given input and output ports. At the same time, there are a number of possible connection combinations (i.e., the number of input and output matrix ports connected to the electric part). The results of experiment 2 show that the propagation paths of the system with input ports #1 and #2 are not a sum of paths for port #1 and port #2 connected separately. The interference between the input waves comes to play making some of the paths inactive. The ability of a huge number of propagation paths can be utilized for building a novel type of combinatorial memory.²⁴ Third, the propagation paths can be recognized with high fidelity by measuring the signal power. There are several possible approaches to the propagation path detection (e.g., using a spectrum analyzer, a go microwave detector, and optical detection methods). The use of $\frac{\omega}{\omega}$ power sensors placed inside the matrix (e.g., ISHE detectors) looks is most promising. The difference in the transmitted power may be $\stackrel{\omega}{=}$ big for different paths. For instance, the data in experiment 3 show a 40 dBm difference in the output power coming from different output ports. This large difference is achieved using frequency filtering. Different propagation paths within the matrix should provide different phase shifts and also support different frequencies of the propagating waves. It may be achieved by applying a local magnetic field to a magnonic waveguide. Fourth, the presented test structure is well-compatible with conventional electronics. VNA and spectrum analyzer were used only at the stage of structure characterization. The electric part requires a broadband amplifier, phase shifters, and attenuators. All of these components can be implemented in a chip. The connection between the magnetic and electric parts is accomplished using micro antennas. It is possible to replace the antennas with more scalable and energetically effi-cient multiferroic elements.³²

Functional throughput is a commonly accepted metric for logic device evaluation.³³ It can be calculated as follows:

Functional throughput
$$\frac{\text{number of operations}}{\text{area time}}$$
: (6)

An act of computation in MARcP is associated with finding a specific path in the given matrix out of many possible. The number



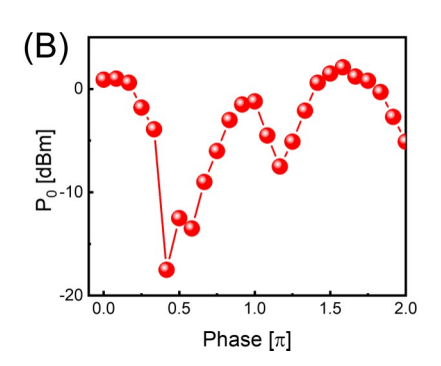


FIG. 16. Experiment 3. (a) Experimental data: the frequency of auto-oscillations in the ring circuit as a function of the external phase shifter Ψ . (b) Experimental data: the power of auto-oscillations P_0 as a function of the external phase shifter Ψ .

of operations is the total number of possible paths that a general computer would check one by one. The number of possible paths scales with the size of the magnonic matrix. Here, we present the estimates for n n square matrix with n input and n output ports. In general, the number of possible paths varies for input/output combination. The largest number of paths is available for the most distant ports (i.e., input port #1 and output port # n) which can be calculated as follows:³⁴

Number of paths (1 input 1 output) $\frac{1}{4}$ (n $\frac{1}{6}$ n)!/(n! n!): (7)

For example, there are 252 possible paths connecting the most distant ports for the 5×5 matrix, as shown in Fig. 1. The number of possible paths just between the most distant ports in the 50×50 matrix exceeds 10^{29} . The total number of paths for all possible combinations of input and output ports can be estimated as follows:

Total number of paths
$$2^{2n}$$
 $(n \nmid n)!/(n! \mid n!)$: (8)

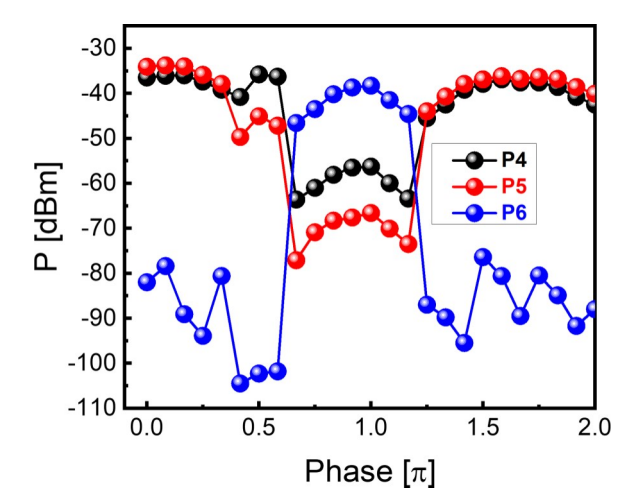


FIG. 17. Experiment 3. Experimental data: the output power measured at the ports as a function of the external phase shifter Ψ . The black, red, and blue curves depict P_4 , P_5 , and P_6 , respectively.

The first term on the right corresponds to the number of input–output port combinations, while the second term is related to the number of paths between the ports. The area of the combinatorial device is mainly defined by the size of the multi-path matrix. It can be estimated as 1^2 n^2 , where 1 is the characteristic size of the mesh cell. The computational time depends on the size of the mesh and the signal group velocity $1 \ n^2/v_g$. The overall, functional throughput of MARcP can be estimated as follows:

Functional throughput (MARcP)
$$\frac{2^{2n} (n \nmid n)!/(n! \mid n!)}{1^2 n^2 1 n/v^2}$$
: (9) g

Regardless of the size of the matrix and the signal propagation speed, the functional throughput increases proportionally to n factorial. It results in an enormous number of paths even for a relatively small structure. For example, taking $1 \% 100 \ \mu m$ and n % 50, one can estimate the area of the device to be 25 mm², the computational time is 25 μ s based 10^4 m/s spin wave group velocity. The functional throughput exceeds 10^{60} operations per meter squared per second. It will take a bit longer than the age of the universe $(13.77 \times 10^9 \ years)$ to check one-by-one all paths (one path per ns) for current supercomputers.

There are certain limits and constraints of MARcP to be discussed. It is a co-processor that can be utilized for specific types of mathematical problems associated with pathfinding. Examples of prime factorization and bridges of the Konigsberg problem are presented in Ref. 24 and reproduced here. Basic operations such as addition and multiplication are more convenient to solve on a regular computer. The fundamental limit to MARcP functional throughput is associated with the maximum number of paths that can be recognized. Ideally, each path should be associated with a distinct signal frequency. It would provide the maximum difference in the output power similar to the results of example 3. In reality, the frequency range is limited by the physical parameters (e.g., different types of spin waves possess certain frequency ranges for propagation²⁸). So, the number of possible paths between the given input/output ports will be limited. On the other hand, there is no limit on the number of input/output ports. The same frequencies can be utilized for not-crossing paths connecting different input/ output ports. Spin wave elements combining properties of a phase shifter and a frequency filter are very attractive for application in MARcP. However, the propagation length of spin waves at room temperature is limited due to fast damping. For instance, the results

presented in this work are obtained for centimeter size YIG structure. A further increase of the number of input/output ports should be done within the same size which is defined by intrinsic damping in the YIG material. At any rate, there is a big room for functional throughput before one will face the fundamental limits.

In this work, we have proposed a concept of a special-type co-processor where an act of computation is associated with path-finding in the mesh of phase shifters and frequency filters. Its general view is shown in Fig. 1(a). It is a 2D mesh with a set of power sensors and multiple inputs/outputs, where each output port is equipped with an individual phase shifter and attenuator. The results of numerical modeling and experiments only show some important steps of the co-processor operation. For instance, only a one-input one-output case has been modeled (see Fig. 2). The results of numerical modeling in Fig. 5 show the change of the signal propagation path depending on the external phase shifter Ψ. The experimental data are obtained for the multi-input/output structure but without internal power detectors. This inconsistency is to be addressed in future works.

There are several interesting directions for further research to be mentioned. It would be of great benefit to use magnonic crystals for signal filtering.³⁵ In this work, we used commercially available filters with just one central bandpass frequency. Magnonic crystals make it possible to modulate transmission on a set of frequencies. It would significantly enhance the frequency filtering between the paths. Multiferroics (e.g., synthetic multiferroics) are of great promise to be used for spin wave modulation²⁷ and also for connecting the magnonic matrix with the electric part. 26 The integration of multiferroics with magnonic waveguides for achieving a prominent phase shift and frequency filtering is a topic that deserves special consideration. We also want to refer to the recently reported nanomagnet reversal by propagating spin waves.³⁶ The switching was observed in ferromagnet/ferrimagnet hybrid structures consisting of Ni₈₁Fe₁₉ nanostripes prepared on top of the YIG film. The ability to switch nanomagnets on top of YIG waveguides using spin waves may significantly simplify the material structure of MARcP, as no additional elements are needed for matrix initialization.

VI. CONCLUSIONS

We described a magnetic special task co-processor based on a multi-path active ring circuit. The principle of operation is based on the inherent ability of the active ring circuit to self-adjust to resonant frequency(s) enabling auto-oscillations. It makes the circuit search for the resonant path out of many possible in the multi-path matrix consisting of spin wave elements acting as phase shifters and frequency filters. The process of self-adjustment is validated by numerical modeling and experiments. There are three types of experiments accomplished on the six-terminal structure consisting of YIG waveguides. The structure was integrated into an active ring circuit. The output power coming to different ports was measured at different positions of the electric phase shifter. In all cases, it was observed that the output power coming to different ports changes prominently with the change of the external phase. The difference in the output power may exceed 40 dBm at room temperature. This property can be exploited for solving special task mathematical

problems such as prime factorization, the Bridges of Konigsberg problem, and the Traveling Salesman Problem. The projected functional throughput of 10^{60} operations per meter squared per second for 50–50 magnetic mesh gives an insight into the enormous computing capabilities of MARcP. Physical limits and technological challenges are also discussed. This work is a first step toward the novel type of combinatorial logic devices which have not been explored. There is a big room for co-processor elaboration by utilizing recent advances in Magnonics such as magnonic crystals. It may pave a road to Moore's Law continuation through the generations of combinatorial devices with a factorial increase of the functional throughput.

ACKNOWLEDGMENTS

This work of M. Balinskiy and A. Khitun was supported in part by the INTEL Corporation, under Award No. 008635, Project director Dr. D. E. Nikonov and by the National Science Foundation (NSF) under Award No. 2006290, Program Officer Dr. S. Basu. The work of Y. Khivintsev, A. Kozhevnikov, Y. Nikulin, V. Sakharov, and Y. Filimonov was carried out in the framework of the Ministry of Science and Higher Education of the Russian Federation state task "Spintronics."

AUTHOR DECLARATIONS

Conflict of Interest

The authors have no conflicts to disclose.

Author Contributions

Mykhaylo Balynsky: Data curation (equal). Yuri Khivintsev: Data curation (equal). Alexander Kozhevnikov: Data curation (equal). Yuri Nikulin: Data curation (equal). Valentin Sakharov: Data curation (equal). Yuri Filimonov: Data curation (equal). Alexander Khitun: Conceptualization (equal); Data curation (equal).

DATA AVAILABILITY

All data generated or analyzed during this study are included in this published article.

REFERENCES

¹X. M. Li and L. D. Xu, "A review of internet of things-resource allocation," IEEE Internet Things J. 8, 8657–8666 (2021).

²H. Perez-Sanchez, J. M. Cecilia, and I. Merelli, in 2nd International Work-Conference on Bioinformatics and Biomedical Engineering (IWBBIO) (Roehampton University Press, 2014), pp. 494–506.

³G. Boole, An Investigation of the Laws of Thought on Which are Founded the Mathematical Theories of Logic and Probabilities (Dover Publications, New York, 1958) (reissued by Cambridge University Press, 2009). 978-1603863155 (1854).

⁴G. E. Moore, "Cramming more components onto integrated circuits," Electronics 38, 114–117 (1965).

⁵M. T. Bohr and I. A. Young, "CMOS scaling trends and beyond," IEEE Micro 37, 20–29 (2017).

⁶B. Hoefflinger, in Chips 2020, Vol. 2 New Vistas in Nanoelectronics Frontiers Collection, edited by B. Hoefflinger (Springer, 2016), pp. 143–148.

- ⁷H. H. Radamson et al., "State of the art and future perspectives in advanced CMOS technology," Nanomaterials 10, 1555 (2020).
- ⁸A. Kelleher, (edited by Intel newsroom), see https://www.intel.com/content/ www/us/en/newsroom/opinion/moore-law-now-and-in-the-future.html#gs.ko wb9b (2022).
- ⁹D. E. Nikonov and I. A. Young, "Overview of beyond-CMOS devices and a uniform methodology for their benchmarking," Proc. IEEE 101, 2498-2533
- ¹⁰S. Manipatruni, D. E. Nikonov, and I. A. Young, "Beyond CMOS computing with spin and polarization," Nat. Phys. 14, 338-343 (2018).
- ¹¹A. Barman et al., "The 2021 magnonics roadmap," J. Phys.: Condens. Matter 33, 413001 (2021).
- ¹²M. P. Kostylev, A. A. Serga, T. Schneider, B. Leven, and B. Hillebrands, "Spin-wave logical gates," Appl. Phys. Lett. 87, 153501 (2005).
- ¹³A. Khitun and K. L. Wang, "Nano scale computational architectures with spin wave bus," Superlattices Microstruct. 38, 184-200 (2005).
- ¹⁴J. L. Chen, H. M. Yu, and G. Gubbiotti, "Unidirectional spin-wave propagation and devices," J. Phys. D: Appl. Phys. 55, 123001 (2022).
- ¹⁵A. Khitun, M. Q. Bao, and K. L. Wang, "Spin wave magnetic nanofabric: A new approach to spin-based logic circuitry," IEEE Trans. Magn. 44, 2141-2152 (2008).
- ¹⁶A. Khitun and I. Krivorotov, Spin Wave Logic Devices (CRC Press, 2019).
- ¹⁷A. B. Ustinov, E. Lahderanta, M. Inoue, and B. A. Kalinikosl, "Nonlinear spinwave logic gates," IEEE Mag. Lett. 10, 5508204 (2019).
- ¹⁸T. Fischer et al., "Experimental prototype of a spin-wave majority gate," Appl. Phys. Lett. 110, 152401 (2017).
- ¹⁹N. Sato, K. Sekiguchi, and Y. Nozaki, "Electrical demonstration of spin-wave logic operation," Appl. Phys. Express 6, 063001 (2013).
- ²⁰K. Nanayakkara, A. Anferov, A. P. Jacob, S. J. Allen, and A. Kozhanov, "Cross junction spin wave logic architecture," IEEE Trans. Magn. 50, 11 (2014).
- ²¹R. Cheng, M. W. Daniels, J. G. Zhu, and D. Xiao, "Antiferromagnetic spin wave field-effect transistor," Sci. Rep. 6, 24223 (2016).
- ²²A. Litvinenko et al., cond-matter archiv (2022).
- ²³S. Watt and M. Kostylev, "Reservoir computing using a spin-wave delay-line active-ring resonator based on yttrium-iron-garnet film," Phys. Rev. Appl. 13, 034057 (2020).

- ²⁴A. Khitun and M. Balinskiy, "Combinatorial logic devices based on a multipath active ring circuit," Sci. Rep. 12, 9482 (2022).
- ²⁵T. J. Silva, C. S. Lee, T. M. Crawford, and C. T. Rogers, "Inductive measurement of ultrafast magnetization dynamics in thin-film permalloy," J. Appl. Phys. 85, 7849-7862 (1999).
- ²⁶S. Cherepov et al., "Electric-field-induced spin wave generation using multiferroic magnetoelectric cells," Appl. Phys. Lett. 104, 082403 (2014).
- ²⁷M. Balinskiy et al., "Magnetoelectric spin wave modulator based on synthetic multiferroic structure," Sci. Rep. 8, 10867 (2018).
- ²⁸A. G. Gurevich and G. A. Melkov, Magnetization Oscillations and Waves (CRC Press, 1996), pp. 147-176.
- ²⁹V. S. Tiberkevich, R. S. Khymyn, H. X. Tang, and A. N. Slavin, "Sensitivity to external signals and synchronization properties of a non-isochronous auto-oscillator with delayed feedback," Sci. Rep. 4, 3873 (2014).
- ³⁰M. Covington, T. M. Crawford, and G. J. Parker, "Time-resolved measurement of propagating spin waves in ferromagnetic thin films," Phys. Rev. Lett. 89, 237202 (2002).
- ³¹J. H. Collins and D. C. Webb, "Magnetoacoustic delay line employing YIG-YAG-YIG configuration," Proc. Inst. Electr. Electron. Eng. 55, 1492
- ³²S. Cherepov et al., "Electric-field-induced spin wave generation using multiferroic magnetoelectric cells," in Proceedings of the 56th Conference on Magnetism and Magnetic Materials (MMM 2011), DB-03, Scottsdale, Arizona (MMM, 2011).
- ³³D. E. Nikonov and I. A. Young, "Uniform methodology for benchmarking beyond-CMOS logic devices," in 2012 IEEE International Electron Devices Meeting (IEDM 2012) (IEDM, 2012), p. 25.
- ³⁴P. Mladenović, Combinatorics: A Problem Based Approach, Problem Books in Mathematics (Springer, Cham, 2019), pp. 55-65.
- ³⁵M. Krawczyk and D. Grundler, "Review and prospects of magnonic crystals and devices with reprogrammable band structure," J. Phys.: Condens. Matter 26,
- 36K. Baumgaertl and D. Grundler. "Reversal of nanomagnets by propagating by magnons in ferrimagnetic yttrium iron garnet enabling nonvolatile magnon memory," arXiv:2208.10923 (2022).